Vanadia-promoted Ru/TiO_2 catalysts for enhanced CO_2 methanation

Plaifa Hongmanorom[1], Ruis Van Eeckhout[1], François Devred, Damien P. Debecker[*]

Institute of Condensed Matter and Nanosciences–Molecular, Solids and Reactivity (IMCN−MOST), Université catholique de Louvain (UCLouvain), Place Louis Pasteur, 1, box L4.01.09, 1348 Louvain-La-Neuve, Belgium.

[1] These authors contributed equally to this work.

[*] Corresponding Author: damien.debecker@uclouvain.be

Abstract

Gaining insight into the role of metal promoters in CO_2 methanation is essential for designing more effective methanation catalysts. In this study, Ru-based catalysts supported on V_2O_5-TiO_2 were prepared via sequential wet impregnation to unravel the origin of the promotional effect of vanadia on Ru/TiO_2 catalysts. Tuning the relative composition of TiO_2 and V_2O_5 allows the synergistic interactions between the support components and Ru nanoparticles to be optimized. At 200 °C, Ru/12%V_2O_5-TiO_2 catalyst achieves CH_4 formation rate of 1.22 $\mu molg_{cat}^{-1}s^{-1}$, outperforming both Ru/TiO_2 and Ru/V_2O_5 catalysts. Its superior activity is attributed to the combined effects of TiO_2, which helps maintaining relatively high Ru dispersion, and V_2O_5, which is reduced by hydrogen spillover from Ru, generating surface oxygen vacancies and hydroxyl groups. The latter species are shown to promote the formation of formate intermediates, while higher Ru dispersion facilitates their decomposition to adsorbed CO prior to hydrogenation to CH_4.

Keyword: Ruthenium; Titania; Vanadia; Promoter; CO_2 methanation

1. Introduction

The rising atmospheric concentration of carbon dioxide (CO_2) from human activities is a major contributor to the increase in global average temperature, approaching the critical threshold of 1.5°C above pre-industrial levels set by the Paris Agreement [1, 2]. CO_2 utilization has been proposed as a promising strategy to address CO_2-induced climate change by converting captured CO_2 into valuable products. In particular, CO_2 conversion with green hydrogen (H_2) to produce methane (CH_4), known as CO_2 methanation or Sabatier reaction, offers potential for CO_2 abatement, renewable energy storage, and clean fuel generation. In the Power-to-Gas (PtG) scenario, green hydrogen produced from surplus renewable electricity reacts with captured CO_2 to generate methane, which can be readily transported through existing natural gas pipelines and utilized either as fuel for heat generation or as feedstock for the synthesis of various chemicals [3-5].

CO_2 methanation is an exothermic reaction that is thermodynamically favorable at low temperatures. However, at these temperatures, the reaction faces kinetic limitations due to the high activation energy required for the eight-electron reduction of CO_2 to CH_4. Therefore, the development of efficient low-temperature CO_2 methanation catalysts is essential [6, 7]. Both noble (Ru, Rh, Pd, and Pt) and non-noble (Ni, Co, and Fe) metals have been investigated as active phases for CO_2 methanation. Among them, Ru offers a good balance, showing higher activity and selectivity than non-noble metal catalysts, particularly at low temperatures, while being less costly than other noble metal catalysts [8-10]. In the literature, various factors, such as Ru particle size and shape [11, 12], support material [13, 14], metal-support interaction [15, 16], and the addition of promoters or dopants [17-20] have been explored to enhance activity and selectivity in CO_2 methanation.

Among metal promoters or dopants, alkali metals (Li, Na, K, and Cs) have been extensively studied, with Na shown to greatly enhance the CO_2 methanation activity of Ru-based catalysts. Based on in-situ DRIFTS experiments and DFT calculations, the electron-donating nature of Na was found to increase the electron density at interfacial Ru sites. This promotes electron back-donation to adsorbed CO intermediates, weakening the C-O bond and thereby facilitating CO dissociation and subsequent hydrogenation toward CH_4 formation [18, 20, 21]. Similarly, Quintana et al. reported that doping Ba, an alkali earth metal, into the lattice of g-C_3N_4 support enhanced the electron-donating properties of nitrogen functionalities and promoted electron transfer from support to Ru species. In-situ DRIFTS showed that CO species strongly bounded to electron-rich Ru sites favored CH_4 formation [22]. In another study on alkaline earth, Cisneros et al. revealed that incorporating MgO into the lattice of a ZrO_2 support promoted the generation of oxygen vacancies/Zr^{3+}, which could enable electron transfer to adjacent Ru sites. This modulated the stability of formate intermediates by weakening O-C-O bond, thereby facilitating formate decomposition and subsequent hydrogenation [19]. To date, little work has been done on the promoting effects of transition metals, with most studies focusing on Ni-based catalysts. Vanadium, in particular, has been shown to enhance the CO_2 methanation activity of Ni phyllosilicate [23], Ni/Al_2O_3 [24, 25], Ni-Mg-Al hydrotalcite-derived [26, 27], and Ni supported on 3D-mesoporous KIT-6 [28] catalysts. In general, this promotion effect was attributed to improved Ni dispersion and increased surface basicity for CO_2 adsorption and activation. Recently, we investigated the promotional effects of Ti, Zr, Nb, and V on mesoporous silica-supported Ru catalysts for CO_2 methanation [29]. We identified that Ru-V synergy enhanced hydrogen spillover and generated oxygen vacancies, which in turn modified CO adsorption and promoted methanation via the CO pathway.

In the present study, we investigated the effect of vanadium on the catalyst properties and catalytic performance of TiO_2-supported Ru catalysts for CO_2 methanation, with particular attention to improving low-temperature activity. Despite the high intrinsic activity of Ru catalysts, their low-temperature performance is strongly influenced by the support, particularly its ability to generate oxygen vacancies and facilitate CO_2 activation. In this context, V_2O_5/TiO_2-based catalysts, well known for their redox properties, offer a promising strategy to enhance CO_2 adsorption and activation at low temperatures. Such systems have been widely employed in various reactions, such as selective catalytic reduction (SCR) of NO_x with NH_3 [30, 31], total oxidation of volatile organic compounds (VOC) [32, 33], and oxidative dehydrogenation (ODH) of alkanes and alcohols [34, 35]. To the best of our knowledge, this is the first report on the use of vanadia-promoted TiO_2 supports in CO_2 hydrogenation, particularly in combination with Ru catalysts. The formation of surface oxygen vacancies and hydroxyl groups on Ru/V_2O_5-TiO_2, linked to enhanced low-temperature CO_2 methanation activity, were unraveled by H_2-TPR, CO_2-TPD, and in-situ DRIFTS experiments.

2. Experimental

2.1. Catalyst preparation

The catalysts were prepared via two successive wet impregnation steps: (i) impregnation of vanadia onto the support, commercially available Degussa P25 TiO_2 powder, and (ii) impregnation of RuO_2 colloidal suspension onto vanadia-promoted TiO_2.

To prepare vanadia-promoted TiO_2 supports, ammonium metavanadate (NH_4VO_3) was first mixed with oxalic acid monohydrate ($H_2C_2O_4.H_2O$) in 50 mL of deionized water to solubilize the vanadium precursor, with a fixed molar ratio $H_2C_2O_4.H_2O/NH_4VO_3$ of 2.33. Then, 5 g of Degussa P25 TiO_2 powder, pre- calcined in air at 500 °C (5 °C/min) for 5 h, was added to the solution. The obtained suspension was heated in an oil bath at 50°C and stirred for 5h. After drying overnight in a vacuum oven at 50°C, the resulting powder was calcined in air at 450°C (5°C/min) for 5h. The amount of NH_4VO_3 added was calculated to obtain x%V_2O_5-TiO_2 (x = 3, 6, 9, 12, or 15, where x represents the weight percent of V_2O_5) after calcination. A pure TiO_2 support was prepared by calcining pristine Degussa P25 TiO_2 powder in air at 500 °C (5 °C/min) for 5 h. A pure V_2O_5 support was also synthesized by dissolving NH_4VO_3 with $H_2C_2O_4.H_2O$ in 50 mL of deionized water, following the same procedure used for preparing vanadia-promoted TiO_2 supports, but without the addition of TiO_2.

The catalysts with a nominal Ru loading of 2wt% were synthesized by wetness impregnation, following the procedure reported by Debecker et al. [36]. The use of colloidal RuO_2 as a precursor in our study was a deliberate synthetic choice, as it provides a highly stable (up to several months at room temperature without further stirring or additives) and monodispersed colloidal suspension of RuO_2 (~2 nm), prepared via a sustainable aqueous oxidative pathway reported in our previous work [37]. First, colloidal suspension of RuO_2 was prepared by dissolving 126 mg of $RuCl_3{\cdot}H_2O$ in 30 mL of deionized water. After stirring for 1 min, 17.25 mL of 14% H_2O_2 was added dropwise. The resulting solution was then incubated at 95°C for 2h. After cooling to room temperature, 3 g of support was added to the suspension, which was stirred for 16 h in an oil bath at 50°C. The mixture was then dried under vacuum using a rotavapor at 50°C and calcined at 450°C (5°C/min) for 16 h which is known to remove residual chlorine. The catalysts were denoted as Ru/TiO_2, Ru/x%V_2O_5-TiO_2 (x = 3, 6, 9, 12, or 15), and Ru/V_2O_5.

2.2. Catalyst characterization

X-ray diffraction (XRD) analyses were performed on a Bruker AXS-D8 Advance diffractometer using Cu Kα radiation at 30 kV and 40 mA. The diffraction patterns were recorded over a 2θ range of 10-60°, with a step size of 0.025° and a step time of 20 s per step. N_2 physisorption was used to evaluate the textural properties of the catalysts. N_2 physisorption isotherms were recorded at -196°C using a Tristar 3000 instrument (Micromeritics). Prior to the analysis, 80 to 100 mg of calcined catalysts were degassed at 150°C to remove physisorbed water and other contaminants. The Brunauer-Emmett-Teller (BET) method was applied to determine the specific surface area in a relative pressure (P/P_0) range of 0.05-0.3.

H_2-temperature programmed reduction (H_2-TPR) and H_2 pulse chemisorption measurements were carried out on a BELCAT II analyzer (Microtrac). For the H_2-TPR measurement, 50 mg of catalyst was pre-treated under a 50 mL/min flow of Ar at 200°C for 1 h, then cooled to 100°C. The H_2-TPR profile was recorded from 100°C to 800°C (heating rate of 10 °C/min) using a 1%H_2/Ar gas mixture (50 mL/min). For the H_2 pulse chemisorption, 150 mg of catalyst was reduced at 300°C for 2 h under a 30 mL/min flow of 5%H_2/Ar, followed by purging with Ar (30 mL/min) for 1h to remove residual H_2. After cooling to 100°C, H_2 was pulsed on the catalyst with a loop volume of 0.989 mL. The amount of surface Ru atoms was calculated based on the amount of chemisorbed H_2, assuming a stoichiometry of H/Ru = 1.

CO_2-temperature programmed desorption (CO_2-TPD) measurement was carried out on a Hiden instrument equipped with an online QGA mass spectrometer (MS). 80 mg of catalyst was first reduced at 300°C under a 30 mL/min flow of 1%H_2/Ar for 2 h, followed by purging with Ar (30 mL/min) for 1 h to remove residual H_2. The catalyst was then cooled to 50°C and exposed to a 15% CO_2/Ar gas stream for 1 h. After flushing with Ar for 30 min, the CO_2-TPD profile was recorded from 50°C to 800°C (heating rate of 10°C/min) under a 30 mL/min Ar flow.

Transmission electron microscopy (TEM) and high-angle annular dark-field scanning transmission electron microscopy (HAADF-STEM), combined with energy-dispersive X-ray spectroscopy (EDX) analysis, were performed at 200 kV using a Talos F200i transmission electron microscope. The software used for the measurements was VELOX.

The weight percentages of Ti, Ru, and V in the vanadia-promoted catalysts were determined by inductively coupled plasma atomic emission spectroscopy (ICP-AES) using an iCAP 6500 instrument (Thermo Scientific). The samples were dissolved via sodium peroxide fusion, ensuing complete dissolution prior to analysis.

X-ray photoelectron spectroscopy (XPS) was carried out using a SSI-X-probe (SSX-100/206) spectrometer equipped with a monochromatized micro-focused Al-Kα X-ray source (1486.6 eV), operated at 10 kV and 20 mA. The C 1s peak was set to 284.8 eV for binding energy calibration. Data processing was carried out using the CasaXPS program (Casa Software Ltd, UK).

In-situ diffuse reflectance infrared Fourier transform spectroscopy (DRIFTS) was performed using a Bruker INVENIO-S spectrometer equipped with a Harrick Praying Mantis chamber. The catalyst was reduced in-situ with H_2 at 300°C for 1 h, followed by purging with He for 30 min. For background subtraction, a spectrum was recorded under He at each temperature. The reaction mixture, consisting of 10%CO_2, 40%H_2, and 50%He, was then introduced into the chamber. Spectra were recorded once a steady state was reached at temperatures from 50°C to 300°C.

2.3. Catalytic test

A continuous flow fixed-bed reactor with an internal size diameter of 6 mm Stainless steel tube was used. 100 mg of catalyst with a particle size of 100-400 μm was first loaded and reduced in situ at 300°C with 20 mL/min flow of H_2 for 2 h, before being purged with a 20 mL/min flow of Ar. The reaction was then operated at 1 atm and temperatures ranging from 200°C to 300°C with a reaction mixture of 20 mL/min (10% CO_2, 40% H_2 and 50% of Ar). Each temperature was maintained for 100 min to allow 5 GC-injections per temperature. The outflow gases were then analyzed using a gas chromatograph (SCION 456-GC) equipped with Hayesep Q, Molsieve 5A, Porapak R and SCION-1 columns. For quantification, a flame ionization detector (FID) was used for CH_4 and a thermal conductivity detector (TCD) for CO_2 and CO. Transfer lines were kept above 120°C to avoid water condensation.

CO_2 conversion (X_{CO_2}), CH_4 selectivity (S_{CH_4}), and CH_4 formation rate (r_{CH_4}) were calculated according to the following equations:

$$X_{CO_2}(\%) = \frac{F_{CO_{2,in}} - F_{CO_{2,out}}}{F_{CO_{2,in}}} \times 100\% \tag{1}$$

$$S_{CH_4}(\%) = \frac{F_{CH_{4,out}}}{F_{CO_{2,in}} - F_{CO_{2,out}}} \times 100\% \tag{2}$$

$$r_{CH_4}(\mu mol_{CH_4} g_{cat}^{-1} s^{-1}) = \frac{F_{CH_{4,out}}}{m_{cat}} \tag{3}$$

where F and m_{cat} are the molar flow rates and mass of catalyst introduced to the reactor, respectively.

3. Results and discussion

3.1. Characterization of supports and corresponding Ru catalysts

The catalysts were prepared by two successive wet impregnations. Vanadia was first impregnated onto TiO_2, followed by RuO_2 impregnation. Both impregnation steps lead to a decrease in specific surface area (Table 1). V_2O_5 and Ru/V_2O_5 display low specific surface areas, consistent with values reported for crystalline V_2O_5 in the literature [38]. N_2 physisorption isotherms of TiO_2, 15%V_2O_5-TiO_2, and their corresponding Ru catalysts are shown as examples in Fig. S1. They exhibit type IV isotherm with H3 hysteresis loop, attributed to interparticle voids formed by the aggregation of non-porous TiO_2 crystallites [39].

The overall isotherm shape remains unchanged after V_2O_5 and RuO_2 impregnation steps, indicating that the textural properties are not significantly altered by these treatments.

Structural properties of TiO_2, V_2O_5-TiO_2, and V_2O_5 supports and their corresponding Ru catalysts were analyzed using XRD (Fig. 1). The commercial P25 TiO_2 exhibits diffraction peaks at 25.4°, 37.0°, 37.8°, 38.6°, 48.1°, 53.9°, and 55.1°, corresponding to anatase TiO_2, and at 27.5°, 36.1°, 41.3°, 44.1°, 54.3°, and 56.7°, corresponding to rutile TiO_2 (Fig. 1(a)) [40]. Diffraction peaks at 15.4°, 20.2°, 26.2°, 31.1°, 32.4°, 34.4° and 51.3°, attributed to the orthorhombic structure of V_2O_5, begin to appear at vanadia loadings of 9 wt% and above [41]. Below this loading, no peaks related to crystalline phases of V_2O_5 are observed, suggesting that the crystallite size is smaller than 5 nm. The peak positions of the TiO_2 phases remain unaffected upon V_2O_5 addition, indicating no distortion of the TiO_2 crystal structure. After RuO_2 impregnation, the XRD diffractograms of the Ru catalysts do not display the main RuO_2 peaks at 27.7° and 35.40°, likely due to overlap with proximate rutile TiO_2 peaks, as well as the low Ru loading (2 wt%) and the small size of RuO_2 particles (< 5 nm) (Fig. 1(b)).

Table 1 Specific surface area (S_{BET}) of TiO_2, V_2O_5-TiO_2, and V_2O_5 supports and their corresponding Ru catalysts.

Support	S_{BET} (m^2/g)	Catalyst	S_{BET} (m^2/g)
TiO_2	49	Ru/TiO_2	42
3%V_2O_5-TiO_2	44	Ru/3%V_2O_5-TiO_2	40
6%V_2O_5-TiO_2	38	Ru/6%V_2O_5-TiO_2	36
9%V_2O_5-TiO_2	38	Ru/9%V_2O_5-TiO_2	30
12%V_2O_5-TiO_2	36	Ru/12%V_2O_5-TiO_2	28
15%V_2O_5-TiO_2	36	Ru/15%V_2O_5-TiO_2	25
V_2O_5	< 5	Ru/V_2O_5	< 5

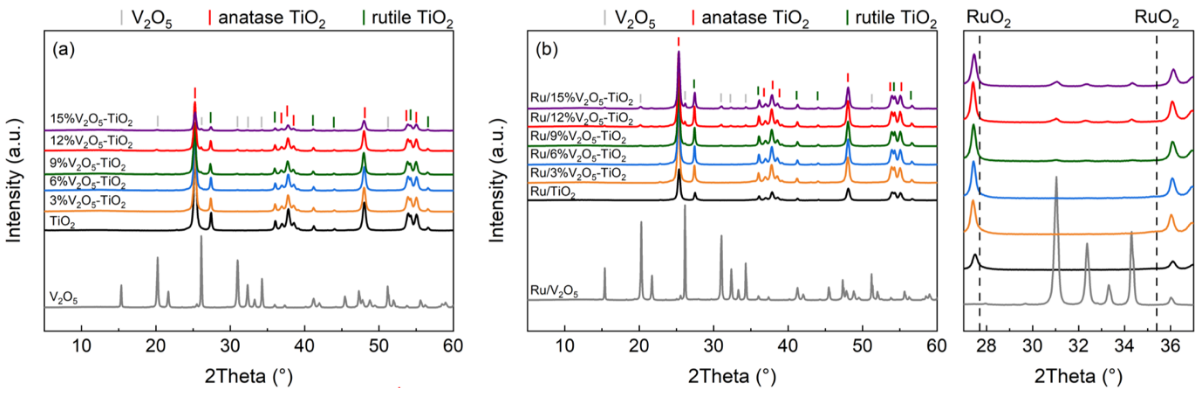

Fig. 1 XRD diffractograms of (a) TiO_2, V_2O_5-TiO_2, and V_2O_5 supports and (b) their corresponding Ru catalysts. An enlarged view of the diffraction region from 27-37° is also shown.

V_2O_5 and Ru contents measured by ICP-AES closely match the nominal loadings, demonstrating the excellent quantitative control during the wet impregnation steps (Table 2). Additionally, HAADF-STEM-EDX images with elemental mapping of Ru/12%V_2O_5-TiO_2 show that vanadia is well dispersed on TiO_2 particles, forming a continuous layer without noticeable isolated V_2O_5 grains (Fig. 2(b)). RuO_2 nanoparticles are also homogeneously dispersed on both Ru/TiO_2 and Ru/12%V_2O_5-TiO_2 catalysts, with no obvious agglomeration observed (Fig. 2). However, the addition of vanadia significantly decreases overall Ru dispersion measured by H_2 pulse chemisorption (Table 2). The highest and lowest dispersion values are observed for Ru/TiO_2 and Ru/V_2O_5, respectively. The Ru dispersion values of the vanadia-doped catalysts fall between these two extremes, suggesting that doping Ru/TiO_2 with vanadia results in a trade-off: the presence of TiO_2 helps maintain relatively high Ru dispersion, partially compensating for the low dispersion observed on pure V_2O_5. It should be noted that H_2 chemisorption on reducible oxide-supported catalysts may be influenced by hydrogen spillover, which can affect the quantitative determination of Ru dispersion. Therefore, the values reported here should be considered approximate and mainly used for qualitative comparison.

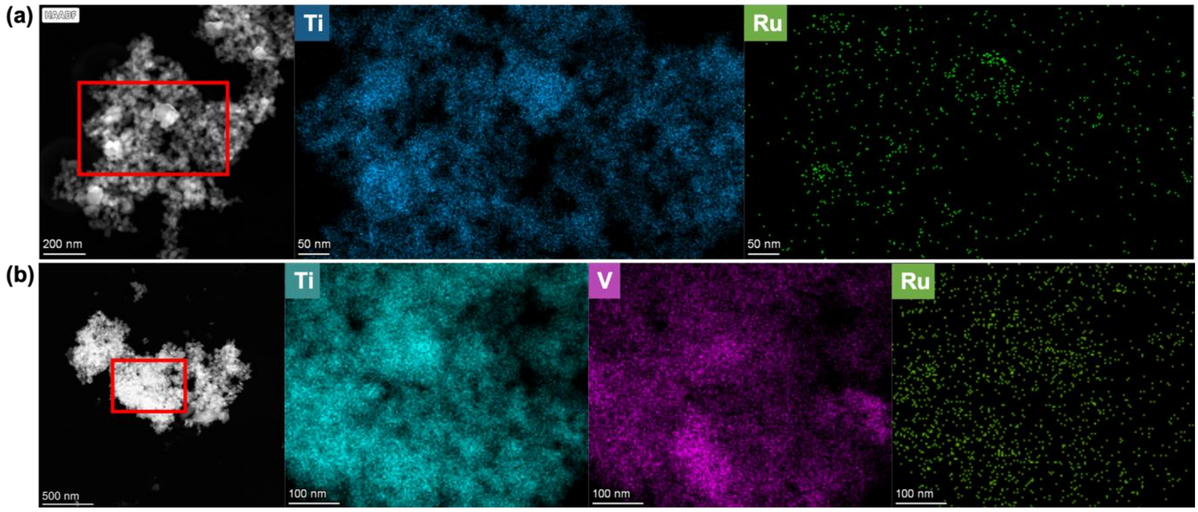

Fig. 2 HAADF-STEM-EDX images with elemental mapping of (a) Ru/TiO_2 and (b) $Ru/12\%V_2O_5$-TiO_2 catalysts (EDX spectra in Fig. S2).

XPS analysis of the freshly calcined catalysts provides information about their chemical state and surface compositions. The Ru 3d and C 1s regions are deconvoluted into three components: metallic Ru^0, oxidized Ru^{4+}, and C 1s. The Ru 3d peaks consist of 3 doublets: an asymmetric peak at 279.7-279.9 eV, corresponding to metallic Ru^0, and a main doublet at 280.5-280.7 eV along with a satellite doublet at 282.4-282.6 eV, both attributed to oxidized Ru^{4+} (Fig. S3) [42]. In Table 3, the atomic V/Ti ratios determined by XPS are much higher than the nominal values (in parentheses), which is consistent with the surface-sensitive nature of XPS technique and with the mode of preparation (i.e. impregnation onto the support surface). As expected, the V/Ti ratio increases with increasing V_2O_5 loading. Additionally, the $Ru^0/(Ru^0+Ru^{4+})$ ratio reveals that Ru is partially present in its metallic form in the fresh catalysts, even though impregnation was done from a RuO_2 colloidal suspension, and subsequent calcination in air was applied. This can be attributed to the ultra- high vacuum (UHV) conditions during XPS analysis, which may induce partial reduction of Ru oxides to metallic Ru. Interestingly, the metallic Ru content decreases from 0.42 for Ru/TiO_2 to 0.04-0.12 for Ru/V_2O_5-TiO_2 catalysts, and no metallic Ru is detected in the Ru/V_2O_5 catalyst. After ex-situ H_2 reduction at 300°C, XPS analysis was also performed (Fig. S4 and Table 3). The results show a slight increase in the proportion of metallic Ru for Ru/TiO_2 and Ru/V_2O_5-TiO_2 catalysts compared to the freshly calcined samples. In contrast, metallic Ru remains undetectable for the Ru/V_2O_5 catalyst, possibly due to surface passivation upon exposure to air during sample transfer. Nevertheless, these results suggest that the presence of V_2O_5 hinders the reduction of RuO_2, likely due to stronger metal-support interaction introduced via vanadia doping, as later evidenced by H_2-TPR results.

Table 2 V_2O_5 and Ru loadings, Ru dispersion, and CH_4 formation rate at 200°C.

Catalyst	ICP-AES		Ru dispersion	CH_4 formation rate
	V_2O_5 (wt%)	Ru (wt%)	(wt%) [a]	(μmol$g_{cat}^{-1}s^{-1}$)
Ru/TiO_2	–	1.5	16.3	0.78
$Ru/3\%V_2O_5$-TiO_2	2.5	1.4	4.9	0.88
$Ru/6\%V_2O_5$-TiO_2	5.4	1.6	4.7	0.87
$Ru/9\%V_2O_5$-TiO_2	7.9	1.7	6.7	1.10
$Ru/12\%V_2O_5$-TiO_2	11.0	1.6	5.3	1.22
$Ru/15\%V_2O_5$-TiO_2	13.8	1.6	4.5	1.10
Ru/V_2O_5	–	1.6	3.2	0.70

[a] Ru dispersion was determined from H_2 pulse chemisorption measurement.

Table 3 XPS analysis results (atomic ratios) of Ru catalysts, experimental H_2 uptake up to 300°C, theoretical H_2 uptake, and the number of weak basic sites for CO_2 adsorption on Ru catalysts.

Catalyst	V/Ti [a]	$Ru^0/(Ru^0+Ru^{4+})$		H_2 uptake up to 300°C (mmol/g)	Theoretical H_2 uptake (mmol/g) [b]	Amount of weak basic sites (mmol/g) [c]
		Calcined	Reduced			
Ru/TiO_2	–	0.42	0.46	0.22	0.30	0.03
$Ru/3\%V_2O_5$-TiO_2	0.13 (0.03)	0.12	0.20	0.42	0.28	0.08
$Ru/6\%V_2O_5$-TiO_2	0.24 (0.06)	0.04	0.08	0.45	0.32	0.12
$Ru/9\%V_2O_5$-TiO_2	0.28 (0.09)	0.04	0.10	0.88	0.34	0.13
$Ru/12\%V_2O_5$-TiO_2	0.28 (0.12)	0.05	0.09	0.94	0.32	0.13
$Ru/15\%V_2O_5$-TiO_2	0.34 (0.15)	0.08	0.10	0.10	0.32	0.14
Ru/V_2O_5	–	0.00	0.00	1.49	0.32	0.01

[a] Nominal bulk V/Ti atomic ratios are provided between parentheses.

[b] The theoretical H_2 uptake was calculated based on the Ru loading measured by ICP, assuming that 2 moles of H_2 are stoichiometrically required to reduce 1 mole of RuO_2.

[c] The deconvoluted peaks are centered between 80°C and 200°C.

H_2-TPR was conducted to investigate the reducibility of the catalysts and to obtain insights on metal-support interactions (Fig. 3(a)). Ru/TiO_2 exhibits a main reduction peak centered at 160°C, corresponding to the reduction of Ru oxides to metallic Ru^0. Increasing the V_2O_5 loading causes this peak to shift toward higher temperatures, indicating that the presence of V_2O_5 strengthens the interaction between RuO_2 and the support, thereby hindering RuO_2 reduction. Ru/V_2O_5 displays broad reduction peaks, attributed to the reduction of both RuO_2 and vanadium oxides. Compared to V_2O_5 and 9%V_2O_5-TiO_2 supports, the H_2-TPR profiles of their respective Ru catalysts show significantly larger reduction peaks at much lower temperatures. This behavior indicates that Ru facilitates the reduction of nearby vanadium species via hydrogen spillover – the migration of dissociated H from Ru to V_2O_5. In addition, H_2 consumption up to 300°C (the reduction temperature) was calculated (Table 3). The values increase with increasing V_2O_5 content and are considerably higher than the theoretical values, except for Ru/15%V_2O_5-TiO_2, whose main reduction peak is centered above 300°C. The increased H_2 consumption further corroborates the reduction of V_2O_5 via hydrogen spillover. These findings are consistent with the literature; for example, Song et al. reported enhanced reducibility of VO_x species and improved redox properties of V-based catalyst in the presence of Ru [43]. Moreover, it has been reported that the reduction of reducible metal oxides via hydrogen spillover from Ru is accompanied by the formation of surface oxygen vacancies and hydroxyl groups [17, 29, 44].

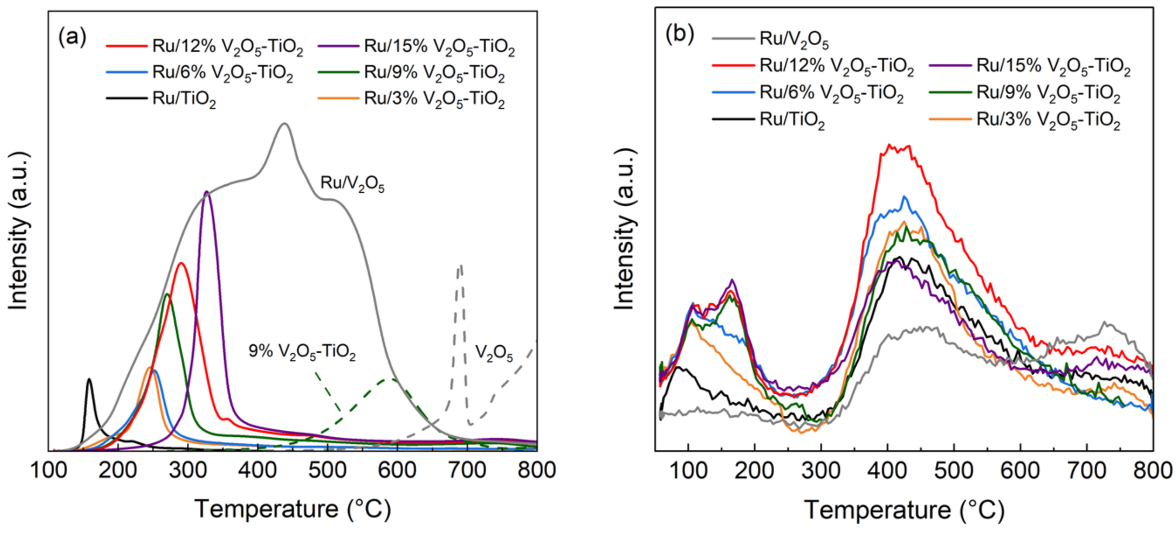

Fig. 3 (a) H_2-TPR profiles of Ru/TiO_2, Ru/V_2O_5-TiO_2, and Ru/V_2O_5 catalysts, compared with those of 9%V_2O_5-TiO_2 and V_2O_5 supports. (b) CO_2-TPD profiles of Ru/TiO_2, Ru/V_2O_5-TiO_2, and Ru/V_2O_5 catalysts.

It is noted that V_2O_5 is generally reported to provide surface acidity [45]. However, in this study, partial reduction of vanadia via hydrogen spillover from Ru occurs under H_2 pre-treatment, and this reduction is expected to decrease surface acidity due to the lower cation charge [46]. Concurrently, this reduction promotes the formation of oxygen vacancies and surface hydroxyl groups. As a result, the presence of partially reduced vanadia also influences CO_2 adsorption behavior, as shown in CO_2-TPD profiles, which can be divided into three regions: 80-200°C, 200-350°C, and > 350°C, corresponding to weak, medium, and strong basic sites, respectively (Fig. 3(b)) [19, 47]. Compared to Ru/TiO_2 and Ru/V_2O_5 catalysts, the desorption peaks in the 80-200°C range, attributed to bicarbonates (b-HCO_3^-), for Ru/V_2O_5-TiO_2 catalysts shift to higher temperatures, indicating enhanced strength of weak basic sites. The amount of CO_2 desorbed in the 80-200°C range was also calculated from the area under the curve and used to estimate the number of weak basic sites on the catalysts (Table 3). Ru/V_2O_5-TiO_2 catalysts exhibit a higher number of weak basic sites than Ru/TiO_2 and Ru/V_2O_5 catalysts. These results demonstrate both increased strength and more abundance of weak basic sites on Ru/V_2O_5-TiO_2 catalysts. It has been reported that surface hydroxyl (–OH) groups can act as weak basic sites and play a crucial role in CO_2 hydrogenation by promoting the formation of intermediate species [48, 49]. The desorption peaks above 350°C, associated with bidentate carbonates (b-CO_3^{2-}) and monodentate carbonates (m-CO_3^{2-}) [47], vary in intensity but not in temperature among the catalysts. Although Ru/V_2O_5-TiO_2 catalysts exhibit a higher amount of desorbed CO_2 in this temperature range than Ru/TiO_2, the species adsorbed on strong basic sites are not expected to actively participate in the reaction at 200-300°C (vide infra in the section 3.4.), as they typically require high temperatures to react [13, 50].

3.2. Catalytic performance

CO_2 methanation was evaluated between 200°C and 300°C, with catalysts pre-reduced under H_2 at 300°C. The reaction conditions were chosen such that CO_2 conversion remained well below thermodynamic equilibrium, allowing for the measurement of intrinsic activity. Negligible diffusional limitations were also confirmed (Fig. S5(a)). Under the tested conditions, all catalysts exhibit 100% CH_4 selectivity, and the addition of vanadia effectively enhances the activity of Ru/TiO_2 (Fig. 4(a)). While Ru/3%V_2O_5-TiO_2 and Ru/6%V_2O_5-TiO_2 show modest improvements, a more pronounced enhancement is observed from Ru/9%V_2O_5-TiO_2 onward, indicating that higher V_2O_5 loadings more effectively promote CO_2 methanation. Considering the peak shift to higher temperatures in the H_2-TPR profiles for catalysts with higher V_2O_5 content, Ru/15%V_2O_5-TiO_2 was also tested after reduction at 350°C (Fig. S5(b)). Although this higher reduction temperature facilitates greater RuO_2-to-Ru^0 conversion, it results in lower catalytic activity compared to reduction at 300 °C, likely due to Ru nanoparticle sintering and consequent loss of Ru active sites. It is worth noting that V_2O_5 proves to be an effective catalyst support for this reaction despite the low Ru dispersion. Ru/V_2O_5 shows activity comparable to Ru/TiO_2 at low temperatures and even superior at higher temperatures. CH_4 formation rate at 200°C is also presented in Table 2. The Ru/12%V_2O_5-TiO_2 catalyst achieves CH_4 formation rate of 1.22 $\mu molg_{cat}^{-1}s^{-1}$, which is ca. 1.6 times higher than that of Ru/TiO_2 catalyst (0.78 $\mu molg_{cat}^{-1}s^{-1}$). The CH_4 formation rate ($mmolg_{Ru}^{-1}s^{-1}$) of Ru/12%V_2O_5-TiO_2 is also compared with those of other Ru-based catalysts reported in the literature (Table S1) [19, 29, 51-56]. Ru/12%V_2O_5-TiO_2 exhibits a comparable or superior CH_4 formation rate under similar conditions.

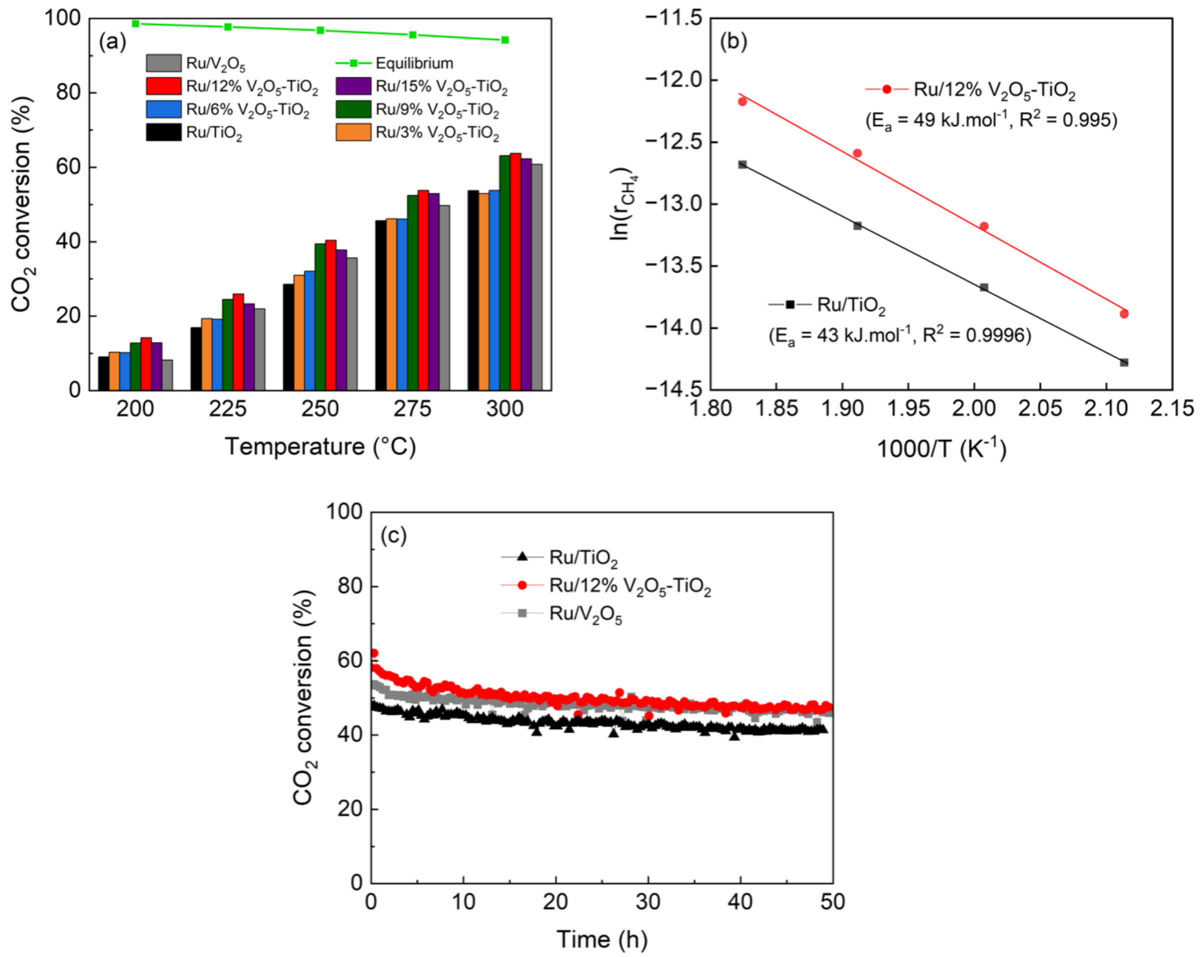

Fig. 4 (a) CO_2 conversion as a function of temperature from 200°C to 300°C. (b) Arrhenius plot of CH_4 formation rate over Ru/TiO_2 and Ru/12%V_2O_5-TiO_2 catalysts in the temperature range of 200-275°C. (c) 50-hour stability test at 300°C of Ru/TiO_2, Ru/12%V_2O_5-TiO_2 and Ru/V_2O_5 catalysts.

To better understand the promoting role of vanadia, the apparent activation energies (E_a) were calculated from the Arrhenius plot in the temperature range of 200-275°C (Fig. 4(b)). The Arrhenius plot was obtained by doubling the total flow rate to 40 mL/min, compared to the standard reaction conditions of 20 mL/min, to lower CO_2 conversion and ensure operation in the kinetic regime (Fig. S5(c)). The E_a values for Ru/TiO_2 and Ru/12%V_2O_5-TiO_2 are 43 kJ/mol and 49 kJ/mol, respectively, which are in the typical range reported for Ru/TiO_2 catalysts in the literature [15, 57]. The similar apparent activation energies of Ru/TiO_2 and Ru/12%V_2O_5-TiO_2 suggest that the addition of V_2O_5 promoter does not alter the reaction mechanism, the nature of the active site, or the rate-limiting step. These findings will be further supported by in-situ DRIFTS experiments in Section 3.4.

A 50-hour stability test at 300°C was performed on Ru/TiO_2, Ru/12%V_2O_5-TiO_2 and Ru/V_2O_5 (Fig. 4(c)). Consistent with the literature, Ru/TiO_2 exhibits relatively stable performance, with CO_2 conversion decreasing from 48% to 41% (less than 10%) over extended periods [58, 59]. In contrast, V_2O_5 has never been used as the catalyst support in CO_2 methanation. Both Ru/12%V_2O_5-TiO_2 and Ru/V_2O_5 show moderate deactivation, with CO_2 conversion dropping from 62% to 48% and from 54% to 45%, respectively, during the first 10 h of reaction. The catalytic performance of Ru/12%V_2O_5-TiO_2 and Ru/V_2O_5 becomes comparable after this initial deactivation period. This suggests that, at 300°C, the advantage of Ru/12%V_2O_5-TiO_2 lies not in enhanced stability, but in achieving similar catalytic performance with a lower vanadium content. Their CH_4 selectivity remains at 100% throughout 50 h test.

3.3. Characterization of spent Ru catalysts

XRD diffractograms of the spent catalysts (Fig. 5(a)) reveal that the crystallinity of TiO_2 in Ru/TiO_2 and Ru/V_2O_5-TiO_2 catalysts remains unchanged after CO_2 methanation between 200-300°C, while peaks associated with the V_2O_5 crystal structure disappear from the spent Ru/x%V_2O_5-TiO_2 (x = 9, 12, and 15) and Ru/V_2O_5 catalysts. New peaks at 27.8°, 37.1°, 42.3°, and 55.6°, corresponding to the monoclinic rutile VO_2 phase, emerge in the XRD pattern of Ru/V_2O_5, indicating that crystalline V_2O_5 is converted to VO_2 during CO_2 hydrogenation [60, 61]. Additionally, a broad peak at 44.8°, attributed to metallic Ru, is observed only in Ru/V_2O_5 [57]. The crystallite size of Ru, estimated using the Scherrer equation, is ca. 6.7 nm. Given the similar Ru loading (2wt%) across all catalysts, the absence of Ru peaks in the other catalysts implies that their Ru crystallite sizes are smaller and fall below the XRD detection limit. It is also possible that the Ru peak overlaps with the rutile TiO_2 peak at 44.1°.

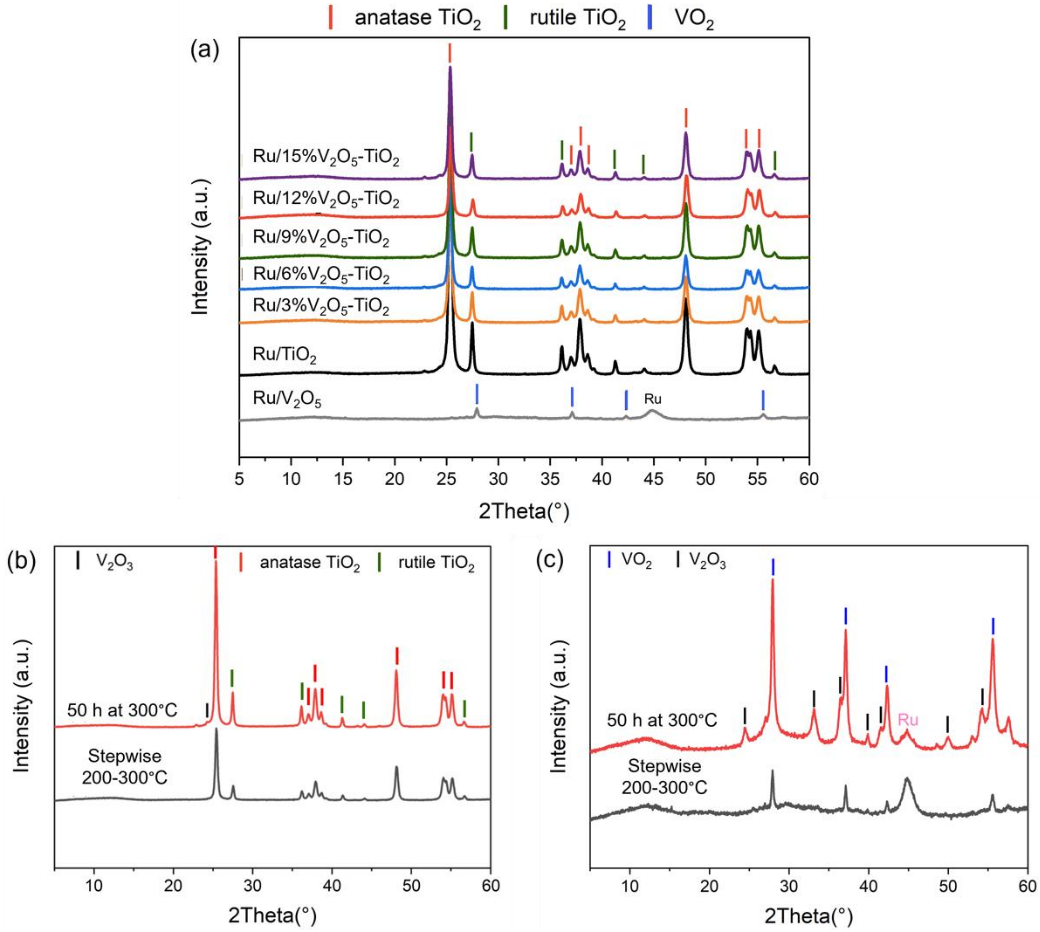

Fig. 5 XRD diffractograms of (a) spent Ru catalysts after the reaction from 200°C to 300°C, (b) spent Ru/12%V_2O_5-TiO_2 after the reaction from 200°C to 300°C and after 50-hour stability test at 300°C, and (c) Ru/V_2O_5 after the reaction from 200°C to 300°C and after 50-hour stability test at 300°C.

Ru/12%V_2O_5-TiO_2 and Ru/V_2O_5 catalysts after 50-h stability test at 300°C were also analyzed by XRD (Fig. 5(b) and (c)). Interestingly, Ru/V_2O_5 exhibits more pronounced VO_2 peaks, along with additional peaks at 24.4°, 33.1°, 36.2°, 39.9°, 41.3°, 49.8° and 54.2°, which are assigned to the corundum structure of V_2O_3 [61, 62]. This demonstrates progressive reduction of V_2O_5 (V^{5+}) to VO_2 (V^{4+}) and subsequently to V_2O_3 (V^{3+}), as well as gradual crystallization of VO_2 and V_2O_3 during the prolonged CO_2 hydrogenation test. These findings align with the work of Corr et al., who performed in-situ XRD experiments during the controlled reduction of vanadium oxides (without Ru) [60]. They reported VO_2 as the dominant crystalline phase after 1 h of reduction at 500°C, and V_2O_3 as the main phase after 6 h. Despite structural transformation of the V_2O_5 support, the Ru crystallite size remains ca. 6.9 nm. Unlike Ru/V_2O_5, VO_2 and V_2O_3 peaks are not clearly observed in the XRD pattern of the spent Ru/12%V_2O_5-TiO_2 after stability test. Their absence may be attributed to lower vanadia content or to overlap with TiO_2 peaks, which could also obscure the reflections from metallic Ru. Based on XRD results of the spent catalysts, the moderate decline in CO_2 conversion observed for vanadia-containing catalysts during 50-h stability test is plausibly associated with structural transformation of vanadia species ($V_2O_5 \rightarrow VO_2 \rightarrow V_2O_3$) under reaction conditions. Significant Ru sintering is unlikely to be the primary cause, as the Ru crystallite size remains small. In addition, given the relatively low reaction temperature (300°C), carbon deposition is expected to be limited [9] and is therefore unlikely to be a major contributor to deactivation.

3.4. In-situ DRIFTS experiments

To gain deeper insight into the promoting effect of vanadia, the evolution of surface intermediate species and the plausible reaction pathway on Ru/TiO_2, $Ru/12\%V_2O_5\text{-}TiO_2$, and Ru/V_2O_5 were investigated using in-situ DRIFTS measurements under CO_2 methanation conditions between 50-300°C (2200-1200 cm^{-1} in Fig. 6). The whole range (4000-1200 cm^{-1}) is also provided in the Supporting Information (Fig. S6) along with additional descriptions.

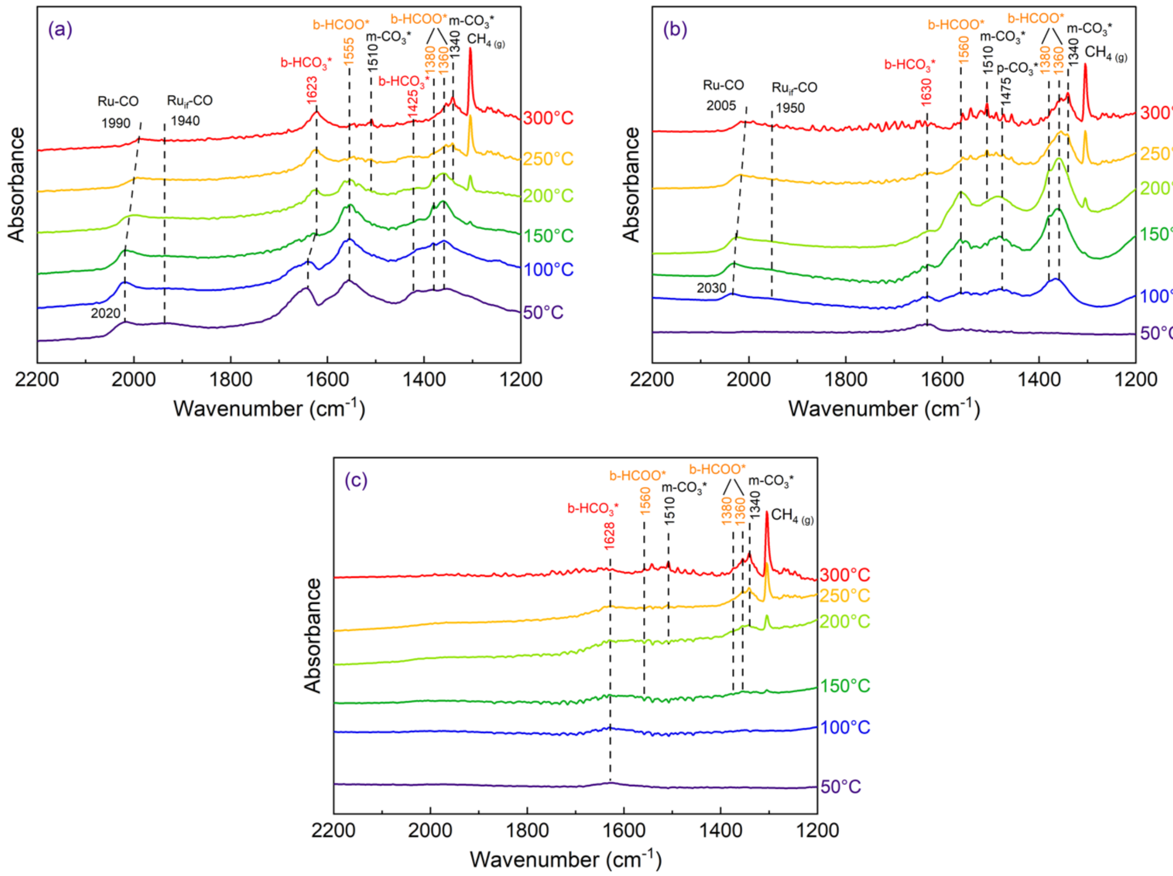

Fig. 6 In-situ DRIFTS spectra (2200-1200 cm^{-1}) recorded at steady-state during CO_2 methanation (10%CO_2, 40%H_2, and 50%He) from 50 °C to 300 °C over (a) Ru/TiO_2, (b) $Ru/12\%V_2O_5\text{-}TiO_2$, and (c) Ru/V_2O_5 catalysts.

In the carbonyl region, no distinct peaks are observed for Ru/V_2O_5 (Fig. 6(c)), whereas bands corresponding to linearly adsorbed CO on Ru sites (Ru-CO at 2030-1990 cm^{-1}) and bridged CO at the metal-support interface (Ru_{if}-CO at 1950-1940 cm^{-1}) [15, 47] appear in the spectra of Ru/TiO_2 and Ru/12%V_2O_5-TiO_2, starting at 50°C and 100°C, respectively (Fig. 6(a) and (b)). With increasing temperature, the Ru-CO band shifts to lower wavenumbers. This red shift may be attributed to the formation of Ru carbonyl hydride species, in which a CO molecule is adsorbed on a Ru atom that also binds one or two hydrogen atoms [63]. In addition to the influence of hydrogen atoms, such a shift accompanied by decreased band intensity may indicate a decrease in CO coverage on metal nanoparticles [64, 65], presumably caused by CO desorption or conversion toward other surface intermediates. However, no gaseous CO bands are detected at 2170 and 2114 cm^{-1} [52]. Instead, the intensity of adsorbed CO bands diminishes and shifts to lower wavenumbers as methane bands at 3014 and 1306 cm^{-1} [66] simultaneously begin to emerge above 150°C, suggesting that CO intermediates undergo hydrogenation to form CH_4.

In the carbonate and formate region, bands at 1630-1623 and 1425 cm^{-1} are assigned to $\nu_{as}(CO_3)$ and $\nu_s(CO_3)$ vibrational modes of bicarbonate species (b-HCO_3^*), respectively [13, 19]. These bands appear as early as 50°C for all three catalysts. Bands at 2873 (Fig. S6), 1560-1555, 1380, and 1360 cm^{-1} (Fig. 6) are attributed to ν(CH), $\nu_{as}(CO_2)$, δ(CH), and $\nu_s(CO_2)$ vibrational modes of bidentate formate species (b-$HCOO^*$) [17, 67], respectively. These b-$HCOO^*$ bands are first observed at 50°C for Ru/TiO_2, 100°C for Ru/12%V_2O_5-TiO_2, and 150°C for Ru/V_2O_5. The intensities of b-$HCOO^*$ bands reach their maxima at 150°C, 200°C, and 300°C, respectively, and coincide with a decrease in the intensity of b-HCO_3^* bands, indicating the conversion of b-HCO_3^* to b-$HCOO^*$. It is known that CO_2 can react with surface hydroxyl groups on the support to form bicarbonate species, which can be hydrogenated to bidentate formate species and subsequently further hydrogenated to produce CH_4 via the formate pathway [17, 50]. Among three catalysts, Ru/12%V_2O_5-TiO_2 exhibits the lowest b-HCO_3^* band intensities and the highest b-$HCOO^*$ band intensities during the stepwise-increasing reaction temperatures. This trend demonstrates that Ru/12%V_2O_5-TiO_2 promotes the conversion of b-HCO_3^* to b-$HCOO^*$. In addition to bicarbonate species, bands associated with monodentate carbonate species (m-CO_3^*) at 1510 and 1340 cm^{-1} are detected for all three catalysts, while polydentate carbonate species (p-CO_3^*) at 1475 cm^{-1} are observed only for Ru/12%V_2O_5-TiO_2 [11, 17]. These carbonate species likely arise from CO_2 adsorption on strongly basic adsorbed O^{2-} sites [13, 67]. Notably, monodentate carbonate species begin to form at 200°C and continue to increase at higher temperatures, suggesting that they do not participate in further transformation into formate intermediates and instead act as spectators.

For Ru/V_2O_5 (Fig. 6(c)), the onset of CH_4 formation occurs at the same temperature at which b-HCOO* species first appear, and the intensity of b-HCOO* bands increases with temperature in parallel with CH_4 formation. In contrast, on Ru/TiO_2 and $Ru/12\%V_2O_5\text{-}TiO_2$, b-$HCOO^*$, bands reach their maximum intensities at lower temperatures (Fig. 6(a) and (b)). Moreover, for both catalysts, the onset of $HCOO^*$ formation coincides with the appearance of their respective carbonyl species. Based on these observations, it is speculated that $HCOO^*$ may also undergo conversion to carbonyl species on Ru/TiO_2 and $Ru/12\%V_2O_5\text{-}TiO_2$. To further examine this possibility, CO_2 adsorption DRIFTS experiments were carried out on $Ru/12\%V_2O_5\text{-}TiO_2$ to determine whether adsorbed CO is formed via direct CO_2 dissociation ($CO_{2(ads)} \rightarrow CO_{(ads)} + O_{(ads)}$) or via H-assisted CO_2 dissociation (Fig. S7(a)). The b-HCO_3^* band at 1625 cm^{-1} is observed at 50 °C and decreases with increasing temperature. Meanwhile Ru-CO species (2076 and 2030 cm^{-1}) appear at 200°C, which is higher than the temperature (100°C) required in the presence of H_2. This observation suggests that b-HCO_3^* species are converted to carbonyl species. Therefore, in the presence of H_2, it is plausible that adsorbed CO originates from formate/carbonate species through H-assisted CO_2 dissociation rather than direct CO_2 dissociation. This pathway is consistent with mechanism previously proposed for Ru/TiO_2 catalysts [21, 63]. After CO_2 adsorption from 50 to 300°C, the feed gas was switched to H_2 (Fig. S7(b)). Upon introducing H_2, the Ru-CO bands gradually decrease in intensity with a slight shift to lower wavenumbers, and a weak CH_4 band of methane appears, indicating the hydrogenation of CO to CH_4.

Based on these findings, we propose that CO_2 methanation on Ru/V_2O_5 proceeds primarily via the formate pathway. Surface hydroxyl groups serve as adsorption sites for CO_2, leading to the formation of bicarbonate species, which are subsequently hydrogenated to bidentate formate intermediates and further converted to CH_4. On Ru/TiO_2 and $Ru/12\%V_2O_5\text{-}TiO_2$, CO_2 methanation likely follows the H-assisted CO_2 dissociation pathway, in which bicarbonate/bidentate formate species decompose to adsorbed CO that migrates from the support surface to adjacent Ru sites. The product CH_4 is then produced through CO hydrogenation.

3.5. Decisive factors governing CO_2 methanation activity

Promotion with vanadium oxide clearly provokes modifications of the properties of the catalyst, as described above. Although no direct proof is presented for molecular-level interactions between the Ru and VO_x phases, characterization data do indicate that such interactions exist in these formulations. The catalytic activity begins to increase substantially starting from Ru/9%V_2O_5-TiO_2 catalyst (Fig. 4(a)). Notably, this loading also corresponds to the first appearance of diffraction peaks attributable to crystalline V_2O_5 in the XRD patterns (Fig. 1(b)), suggesting that bulk V_2O_5 crystallites larger than ~5 nm more effectively promote the reaction. The highest Ru dispersion is observed for Ru/TiO_2, and the lowest for Ru/V_2O_5 (Table 2), with the Ru/V_2O_5-TiO_2 catalysts falling in between. This indicates that TiO_2 favors the formation of well-dispersed Ru nanoparticles, while V_2O_5 contributes additional promoting effects relevant to enhanced CO_2 methanation.

DRIFTS analyses (Fig. 6) show that higher Ru dispersion on Ru/TiO_2 and Ru/12%V_2O_5-TiO_2 facilitates the decomposition of formate species to adsorbed CO, whereas such decomposition is negligible on Ru/V_2O_5, which has the lowest Ru dispersion. This behavior is likely related to the fact that formate decomposition to adsorbed CO occurs preferentially at the metal-support interface [13, 21]. Higher Ru dispersion, which is associated with a greater number of interfacial sites, could therefore promote the decomposition of formate species located near the interface and the subsequent migration of the resulting adsorbed CO to adjacent Ru sites prior to their hydrogenation to CH_4.

The remaining question is what role V_2O_5 plays in enabling Ru/12%V_2O_5-TiO_2 to outperform Ru/TiO_2. H_2-TPR analyses (Fig. 3(a)) suggest hydrogen spillover from Ru to nearby V_2O_5, while CO_2-TPD analyses (Fig. 3(b)) demonstrate enhanced basicity, particularly stronger and more abundant weak basic sites associated with surface hydroxyl groups on Ru/V_2O_5-TiO_2 catalysts. Taken together, these results suggest that hydrogen spillover to V_2O_5 generates V^{4+}/V^{3+}, surface oxygen vacancies, and hydroxyl groups synchronously, which are beneficial for the formation of bicarbonate and formate species. DRIFTS analyses further show that although the same surface intermediate species are detected on Ru/TiO_2 and Ru/12%V_2O_5-TiO_2 catalysts during the stepwise temperature increase (Fig. 6(a) and (b)), the hydrogenation of bicarbonate to bidentate formate species is significantly enhanced on Ru/12%V_2O_5-TiO_2. This enhancement correlates with its superior CO_2 methanation activity. This finding aligns well with literature reports that the CH_4 formation rate is directly linked to the formation of formate species, which is favored on supports enriched in oxygen vacancies and hydroxyl groups [13, 17, 44].

Overall, tuning the relative composition of TiO_2 and V_2O_5 allows the synergistic interactions between the support components and Ru nanoparticles to be optimized, thereby enhancing CO_2 methanation activity.

4. Conclusions

Model Ru/x%V_2O_5-TiO_2 (x = 3, 6, 9, 12, and 15 wt.%) catalysts were synthesized via two successive wet impregnation steps, with Ru/TiO_2 and Ru/V_2O_5 as reference catalysts. N_2 physisorption and XRD analyses show that the textural and structural properties of P25 TiO_2 remain largely unchanged after V_2O_5 and RuO_2 deposition. HAADF-STEM-EDX further reveals that V_2O_5 is well-dispersed on TiO_2 particles and that RuO_2 nanoparticles are homogeneously distributed on the 12%V_2O_5-TiO_2 support. However, increasing V_2O_5 loading leads to a clear trade-off with Ru dispersion. The presence of TiO_2 helps maintain relatively high Ru dispersion, partly compensating for the low dispersion observed on pure V_2O_5. Despite the reduced Ru dispersion, Ru/12%V_2O_5-TiO_2 catalyst achieves CH_4 formation rate of 1.22 $\mu molg_{cat}^{-1}s^{-1}$, approximately 1.6-fold higher than that of Ru/TiO_2 catalyst (0.78 $\mu molg_{cat}^{-1}s^{-1}$). This enhanced activity is rationalized by synergistic interactions between the support components and Ru nanoparticles. TiO_2 contributes by preserving relatively high Ru dispersion, while hydrogen spillover from Ru to adjacent V_2O_5 facilitates the generation of surface oxygen vacancies and hydroxyl groups, as indicated by H_2-TPR and CO_2-TPD analyses. In-situ DRIFTS analyses further demonstrate that enriched surface oxygen vacancies and hydroxyl groups promote the formation of formate intermediates, while higher Ru dispersion facilitates their subsequent decomposition to adsorbed CO prior to hydrogenation to CH_4.

Acknowledgements

Results presented were made possible thanks to infrastructure acquired under Measure BE-C[C72]-I[I-711], Research Platform for Energy Transition of the French Community of Belgium, funded through the REPowerEU chapter of the NextGenerationEU plan. The FSR (UCLouvain) is also acknowledged for having completed the funding, as the technological platform SUCH of IMCN. This work is also supported by the FNRS under Grant GEQ (Large Equipment) – UG01622F. Plaifa Hongmanorom thanks the Fonds De La Recherche Scientifique – FNRS (10.13039/501100002661) for her postdoctoral researcher – CR fellowship.

References

[1] M. Filonchyk, M.P. Peterson, L. Zhang, V. Hurynovich, Y. He, Greenhouse gases emissions and global climate change: Examining the influence of CO2, CH4, and N2O, Sci. Total Environ., 935 (2024) 173359.
[2] A. Jarvis, P.M. Forster, Estimated human-induced warming from a linear temperature and atmospheric CO2 relationship, Nature Geoscience, 17 (2024) 1222-1224.
[3] M. Götz, J. Lefebvre, F. Mörs, A. McDaniel Koch, F. Graf, S. Bajohr, R. Reimert, T. Kolb, Renewable Power-to-Gas: A technological and economic review, Renewable Energy, 85 (2016) 1371-1390.
[4] M. Thema, F. Bauer, M. Sterner, Power-to-Gas: Electrolysis and methanation status review, Renew. Sustain. Energy Rev., 112 (2019) 775-787.
[5] M.M.F. Hasan, L.M. Rossi, D.P. Debecker, K.C. Leonard, Z. Li, B.C.E. Makhubela, C. Zhao, A. Kleij, Can CO2 and Renewable Carbon Be Primary Resources for Sustainable Fuels and Chemicals?, ACS Sustainable Chem. Eng., 9 (2021) 12427-12430.
[6] L. Shen, J. Xu, M. Zhu, Y.-F. Han, Essential Role of the Support for Nickel-Based CO2 Methanation Catalysts, ACS Catal., 10 (2020) 14581-14591.
[7] J. Ashok, S. Pati, P. Hongmanorom, Z. Tianxi, C. Junmei, S. Kawi, A review of recent catalyst advances in CO2 methanation processes, Catal. Today, (2020).
[8] M. Tommasi, S.N. Degerli, G. Ramis, I. Rossetti, Advancements in CO2 methanation: A comprehensive review of catalysis, reactor design and process optimization, Chem. Eng. Res. Des., 201 (2024) 457-482.
[9] C. Shen, M. Liu, S. He, H. Zhao, C.-j. Liu, Advances in the studies of the supported ruthenium catalysts for CO2 methanation, Chinese Journal of Catalysis, 63 (2024) 1-15.
[10] L.H. Vieira, L.F. Rasteiro, C.S. Santana, G.L. Catuzo, A.H.M. da Silva, J.M. Assaf, E.M. Assaf, Noble Metals in Recent Developments of Heterogeneous Catalysts for CO2 Conversion Processes, ChemCatChem, 15 (2023) e202300493.
[11] Y. Guo, S. Mei, K. Yuan, D.-J. Wang, H.-C. Liu, C.-H. Yan, Y.-W. Zhang, Low-Temperature CO2 Methanation over CeO2-Supported Ru Single Atoms, Nanoclusters, and Nanoparticles Competitively Tuned by Strong Metal–Support Interactions and H-Spillover Effect, ACS Catal., 8 (2018) 6203-6215.
[12] J.H. Kwak, L. Kovarik, J. Szanyi, CO2 Reduction on Supported Ru/Al2O3 Catalysts: Cluster Size Dependence of Product Selectivity, ACS Catal., 3 (2013) 2449-2455.
[13] M.P. Almeida, L.V. Mattos, S. Walker, M. Ayala, C.D. Watson, G. Jacobs, R.C. Rabelo-Neto, M. Akri, S. Paul, F.B. Noronha, Unveiling the effect of support on the mechanism of CO2 hydrogenation over supported Ru catalysts, Applied Catalysis B: Environment and Energy, 365 (2025) 124986.
[14] J.A.H. Dreyer, P. Li, L. Zhang, G.K. Beh, R. Zhang, P.H.L. Sit, W.Y. Teoh, Influence of the oxide support reducibility on the CO2 methanation over Ru-based catalysts, Appl. Catal., B, 219 (2017) 715-726.
[15] J. Zhou, Z. Gao, G. Xiang, T. Zhai, Z. Liu, W. Zhao, X. Liang, L. Wang, Interfacial compatibility critically controls Ru/TiO2 metal-support interaction modes in CO2 hydrogenation, Nature Communications, 13 (2022) 327.

[16] A. Kim, D.P. Debecker, F. Devred, V. Dubois, C. Sanchez, C. Sassoye, CO2 methanation on Ru/TiO2 catalysts: On the effect of mixing anatase and rutile TiO2 supports, Appl. Catal., B, 220 (2018) 615-625.
[17] X. Xu, L. Liu, Y. Tong, X. Fang, J. Xu, D.-e. Jiang, X. Wang, Facile Cr3+-Doping Strategy Dramatically Promoting Ru/CeO2 for Low-Temperature CO2 Methanation: Unraveling the Roles of Surface Oxygen Vacancies and Hydroxyl Groups, ACS Catal., 11 (2021) 5762-5775.
[18] M. Gao, J. Zhang, P. Zhu, X. Liu, Z. Zheng, Unveiling the origin of alkali metal promotion in CO2 methanation over Ru/ZrO2, Appl. Catal., B, 314 (2022) 121476.
[19] S. Cisneros, L. Santa-Taborda, L. Martínez Quintana, A.I.M. Rabee, H. Abed, N. Rockstroh, S. Bartling, M. Romero-Sáez, H. Atia, A. Belén Dongil, A. Brückner, J. Rabeah, The effect of O-vacancies on intermediates stability and electron delocalization over MgO modified Ru/ZrO2: Spectroscopic insights during CO2 methanation, Chem. Eng. J., 474 (2023) 145646.
[20] A. Petala, P. Panagiotopoulou, Methanation of CO2 over alkali-promoted Ru/TiO2 catalysts: I. Effect of alkali additives on catalytic activity and selectivity, Appl. Catal., B, 224 (2018) 919-927.
[21] P. Panagiotopoulou, Methanation of CO2 over alkali-promoted Ru/TiO2 catalysts: II. Effect of alkali additives on the reaction pathway, Appl. Catal., B, 236 (2018) 162-170.
[22] L.M. Quintana, T.H. Vuong, A.I.M. Rabee, J. Rabeah, A.B. Dongil, Effect of Ba and Mg as promoter on Ru/g-C3N4 catalyst for CO2 methanation, J. CO2 Util., 99 (2025) 103158.
[23] Y. Zhang, Y. Chen, Q. Liu, Green synthesis of MCM-41 derived from renewable biomass and construction of VOx-Modified nickel phyllosilicate catalyst for CO2 methanation, Int. J. Hydrogen Energy, 46 (2021) 32003-32016.
[24] G. Garbarino, P. Kowalik, P. Riani, K. Antoniak-Jurak, P. Pieta, A. Lewalska-Graczyk, W. Lisowski, R. Nowakowski, G. Busca, I.S. Pieta, Improvement of Ni/Al2O3 Catalysts for Low-Temperature CO2 Methanation by Vanadium and Calcium Oxide Addition, Industrial & Engineering Chemistry Research, 60 (2021) 6554-6564.
[25] I.S. Pieta, A. Lewalska-Graczyk, P. Kowalik, K. Antoniak-Jurak, M. Krysa, A. Sroka-Bartnicka, A. Gajek, W. Lisowski, D. Mrdenovic, P. Pieta, R. Nowakowski, A. Lew, E.M. Serwicka, CO2 Hydrogenation to Methane over Ni-Catalysts: The Effect of Support and Vanadia Promoting, Catalysts, 11 (2021) 433.
[26] P. Summa, K. Świrk, D. Wierzbicki, M. Motak, I. Alxneit, M. Rønning, P. Da Costa, Co-Precipitated Ni-Mg-Al Hydrotalcite-Derived Catalyst Promoted with Vanadium for CO2 Methanation, Molecules, 26 (2021) 6506.
[27] K. Świrk Da Costa, P. Summa, D. Wierzbicki, M. Motak, P. Da Costa, Vanadium promoted Ni(Mg,Al)O hydrotalcite-derived catalysts for CO2 methanation, Int. J. Hydrogen Energy, 46 (2021) 17776-17783.
[28] H. Cao, W. Wang, T. Cui, H. Wang, G. Zhu, X. Ren, Enhancing CO2 Hydrogenation to Methane by Ni-Based Catalyst with V Species Using 3D-mesoporous KIT-6 as Support, Energies, 13 (2020) 2235.
[29] P. Hongmanorom, A. Neraud, A. Styskalik, W. Limphirat, P. Praserthdam, D.P. Debecker, Metal oxide-promoted mesoporous silica as support for Ru-based CO2 methanation catalysts, Applied Catalysis B: Environment and Energy, 384 (2026) 126142.
[30] W. Si, H. Liu, T. Yan, H. Wang, C. Fan, S. Xiong, Z. Zhao, Y. Peng, J. Chen, J. Li, Sn-doped rutile TiO2 for vanadyl catalysts: Improvements on activity and stability in SCR reaction, Appl. Catal., B, 269 (2020) 118797.

[31] R. Yin, J. Chen, L. Shan, J. Shi, K. Yang, H. Liu, J. Li, Prominent difference in the deactivation rate and mechanism of V2O5/TiO2 under H2S or SO2 during selective catalytic reduction of NOx with NH3, Appl. Catal., B, 328 (2023) 122529.
[32] D.P. Debecker, K. Bouchmella, R. Delaigle, P. Eloy, C. Poleunis, P. Bertrand, E.M. Gaigneaux, P.H. Mutin, One-step non-hydrolytic sol–gel preparation of efficient V2O5-TiO2 catalysts for VOC total oxidation, Appl. Catal., B, 94 (2010) 38-45.
[33] C. Gannoun, A. Turki, H. Kochkar, R. Delaigle, P. Eloy, A. Ghorbel, E.M. Gaigneaux, Elaboration and characterization of sulfated and unsulfated V2O5/TiO2 nanotubes catalysts for chlorobenzene total oxidation, Appl. Catal., B, 147 (2014) 58-64.
[34] A. Zabilska, A.H. Clark, B.M. Moskowitz, I.E. Wachs, Y. Kakiuchi, C. Copéret, M. Nachtegaal, O. Kröcher, O.V. Safonova, Redox Dynamics of Active VOx Sites Promoted by TiOx during Oxidative Dehydrogenation of Ethanol Detected by Operando Quick XAS, JACS Au, 2 (2022) 762-776.
[35] K. Routray, K.R.S.K. Reddy, G. Deo, Oxidative dehydrogenation of propane on V2O5/Al2O3 and V2O5/TiO2 catalysts: understanding the effect of support by parameter estimation, Appl. Catal., A, 265 (2004) 103-113.
[36] D.P. Debecker, B. Farin, E.M. Gaigneaux, C. Sanchez, C. Sassoye, Total oxidation of propane with a nano-RuO2/TiO2 catalyst, Appl. Catal., A, 481 (2014) 11-18.
[37] C. Sassoye, G. Muller, D.P. Debecker, A. Karelovic, S. Cassaignon, C. Pizarro, P. Ruiz, C. Sanchez, A sustainable aqueous route to highly stable suspensions of monodispersed nano ruthenia, Green Chem., 13 (2011) 3230-3237.
[38] K. Omata, T. Nambu, H. Yoshinaga, Ammonia decomposition over vanadium oxide supported Ni catalyst for hydrogen production, Int. J. Hydrogen Energy, 68 (2024) 449-452.
[39] H. Hayashi, K. Torii, Hydrothermal synthesis of titania photocatalyst under subcritical and supercritical water conditions, J. Mater. Chem., 12 (2002) 3671-3676.
[40] M. Umair, A. Ruiz-Aguirre, I. Berruti, S.M. Rodríguez, L. Palmisano, V. Loddo, M. Bellardita, Biomass derivatives photoreforming in pilot plant scale to obtain H2 under green conditions by using ball milling Cu2O-TiO2 P25 photocatalysts, Chem. Eng. J., 504 (2025) 158585.
[41] K.M. Shafeeq, V.P. Athira, C.H.R. Kishor, P.M. Aneesh, Structural and optical properties of V2O5 nanostructures grown by thermal decomposition technique, Appl. Phys. A, 126 (2020) 586.
[42] S. Carenco, C. Sassoye, M. Faustini, P. Eloy, D.P. Debecker, H. Bluhm, M. Salmeron, The Active State of Supported Ruthenium Oxide Nanoparticles during Carbon Dioxide Methanation, J. Phys. Chem. C, 120 (2016) 15354-15361.
[43] Z. Song, Y. Peng, X. Zhao, H. Liu, C. Gao, W. Si, J. Li, Roles of Ru on the V2O5–WO3/TiO2 Catalyst for the Simultaneous Purification of NOx and Chlorobenzene: A Dechlorination Promoter and a Redox Inductor, ACS Catal., 12 (2022) 11505-11517.
[44] F. Wang, S. He, H. Chen, B. Wang, L. Zheng, M. Wei, D.G. Evans, X. Duan, Active Site Dependent Reaction Mechanism over Ru/CeO2 Catalyst toward CO2 Methanation, Journal of the American Chemical Society, 138 (2016) 6298-6305.
[45] I.E. Wachs, Y. Chen, J.-M. Jehng, L.E. Briand, T. Tanaka, Molecular structure and reactivity of the Group V metal oxides, Catal. Today, 78 (2003) 13-24.
[46] T. Kataoka, J.A. Dumesic, Acidity of unsupported and silica-supported vanadia, molybdena, and titania as studied by pyridine adsorption, J. Catal., 112 (1988) 66-79.

[47] M. Liu, R. Zou, C.-j. Liu, Improvement in the activity of Ru/ZrO2 for CO2 methanation by the enhanced hydrophilicity of zirconia, Applied Catalysis B: Environment and Energy, 360 (2025) 124549.
[48] P. Hongmanorom, J. Ashok, G. Zhang, Z. Bian, M.H. Wai, Y. Zeng, S. Xi, A. Borgna, S. Kawi, Enhanced performance and selectivity of CO2 methanation over phyllosilicate structure derived Ni-Mg/SBA-15 catalysts, Appl. Catal., B, (2020) 119564.
[49] F. Han, Q. Liu, D. Li, J. Ouyang, An emerging and high-performance sepiolite-supported Ni catalyst for low-temperature CO2 methanation: The critical role of hydroxyl groups, Journal of Environmental Chemical Engineering, 11 (2023) 110331.
[50] Q. Pan, J. Peng, T. Sun, S. Wang, S. Wang, Insight into the reaction route of CO2 methanation: Promotion effect of medium basic sites, Catal. Commun., 45 (2014) 74-78.
[51] P. Hongmanorom, V. Smeets, A. Neraud, A. Styskalik, P. Praserthdam, C. Copéret, D.P. Debecker, Promotional effect of Ti on mesoporous silica-supported Ru catalysts for CO2 methanation, Materials Today Chemistry, 49 (2025) 103026.
[52] S. Cisneros, S. Chen, C. Fauth, A.M. Abdel-Mageed, S. Pollastri, J. Bansmann, L. Olivi, G. Aquilanti, H. Atia, J. Rabeah, M. Parlinska-Wojtan, A. Brückner, R.J. Behm, Controlling the selectivity of high-surface-area Ru/TiO2 catalysts in CO2 reduction - modifying the reaction properties by Si doping of the support, Appl. Catal., B, 317 (2022) 121748.
[53] H.T.T. Nguyen, Y. Kumabe, S. Ueda, K. Kan, M. Ohtani, K. Kobiro, Highly durable Ru catalysts supported on CeO2 nanocomposites for CO2 methanation, Appl. Catal., A, 577 (2019) 35-43.
[54] S. Cimino, F. Boccia, L. Lisi, Effect of alkali promoters (Li, Na, K) on the performance of Ru/Al2O3 catalysts for CO2 capture and hydrogenation to methane, J. CO2 Util., 37 (2020) 195-203.
[55] A. Rontogianni, N. Chalmpes, E. Nikolaraki, G. Botzolaki, A. Androulakis, A. Stratakis, P. Zygouri, D. Moschovas, A. Avgeropoulos, M.A. Karakassides, D.P. Gournis, S. Tsatsos, G. Kyriakou, N.K. Boukos, P. Panagiotopoulou, I.V. Yentekakis, Efficient CO2 hydrogenation over mono- and bi-metallic RuNi/MCM-41 catalysts: Controlling CH4 and CO products distribution through the preparation method and/or partial replacement of Ni by Ru, Chem. Eng. J., 474 (2023) 145644.
[56] M. Zieliński, E. Janiszewska, A. Drewniak, M. Pietrowski, Methanation of CO2 over Ruthenium Supported on Alkali-Modified Silicalite-1 Catalysts, Molecules, 28 (2023) 6376.
[57] T. Abe, M. Tanizawa, K. Watanabe, A. Taguchi, CO2 methanation property of Ru nanoparticle-loaded TiO2 prepared by a polygonal barrel-sputtering method, Energy Environ. Sci., 2 (2009) 315-321.
[58] A.M. Abdel-Mageed, K. Wiese, M. Parlinska-Wojtan, J. Rabeah, A. Brückner, R.J. Behm, Encapsulation of Ru nanoparticles: Modifying the reactivity toward CO and CO2 methanation on highly active Ru/TiO2 catalysts, Appl. Catal., B, 270 (2020) 118846.
[59] Z. Zhao, Q. Jiang, Q. Wang, M. Wang, J. Zuo, H. Chen, Q. Kuang, Z. Xie, Effect of Rutile Content on the Catalytic Performance of Ru/TiO2 Catalyst for Low-Temperature CO2 Methanation, ACS Sustainable Chem. Eng., 9 (2021) 14288-14296.
[60] S.A. Corr, M. Grossman, J.D. Furman, B.C. Melot, A.K. Cheetham, K.R. Heier, R. Seshadri, Controlled Reduction of Vanadium Oxide Nanoscrolls: Crystal Structure, Morphology, and Electrical Properties, Chem. Mater., 20 (2008) 6396-6404.
[61] B.-T. Liu, X.-M. Shi, X.-Y. Lang, L. Gu, Z. Wen, M. Zhao, Q. Jiang, Extraordinary pseudocapacitive energy storage triggered by phase transformation in hierarchical vanadium oxides, Nature Communications, 9 (2018) 1375.

[62] K. Wu, Y. Wu, P. Fu, D. Yang, B. Ruan, M. Wu, R. Wu, Composites of Vanadium (III) Oxide (V_2O_3) Incorporating with Amorphous C as Pt-Free Counter Electrodes for Low-Cost and High-Performance Dye-Sensitized Solar Cells, ACS Omega, 6 (2021) 11183-11191.
[63] J. Xu, X. Su, H. Duan, B. Hou, Q. Lin, X. Liu, X. Pan, G. Pei, H. Geng, Y. Huang, T. Zhang, Influence of pretreatment temperature on catalytic performance of rutile TiO_2-supported ruthenium catalyst in CO_2 methanation, J. Catal., 333 (2016) 227-237.
[64] A. Karelovic, P. Ruiz, Mechanistic study of low temperature CO_2 methanation over Rh/TiO_2 catalysts, J. Catal., 301 (2013) 141-153.
[65] S. Chen, A.M. Abdel-Mageed, M. Li, S. Cisneros, J. Bansmann, J. Rabeah, A. Brückner, A. Groß, R.J. Behm, Electronic metal-support interactions and their promotional effect on CO_2 methanation on Ru/ZrO_2 catalysts, J. Catal., 400 (2021) 407-420.
[66] P. Hongmanorom, J. Ashok, P. Chirawatkul, S. Kawi, Interfacial synergistic catalysis over Ni nanoparticles encapsulated in mesoporous ceria for CO_2 methanation, Appl. Catal., B, 297 (2021) 120454.
[67] X. Jia, X. Zhang, N. Rui, X. Hu, C.-j. Liu, Structural effect of Ni/ZrO_2 catalyst on CO_2 methanation with enhanced activity, Appl. Catal., B, 244 (2019) 159-169.